Influence of carrier localization on photoluminescence emission from sub-monolayer quantum dot layers

T.-Y. Huang,[1,a)] T. Borrely,[2,3,a)] Y.-C. Yang,[1] A. Alzeidan,[3] G. M. Jacobsen,[4] M. D. Teodoro,[4] A. A. Quivy,[3] and R. S. Goldman[1,2,b)]

[1]*Department of Materials Science & Engineering, University of Michigan, Ann Arbor, MI 48109-2136, USA*

[2]*Department of Physics, University of Michigan, Ann Arbor, MI 48109-2136, USA*

[3]*Institute of Physics, University of São Paulo, São Paulo, SP 05508-090, Brazil*

[4]*Department of Physics, Federal University of São Carlos, São Carlos, SP 13565-905, Brazil*

[a)]T.-Y. Huang and T. Borrely contributed equally to this work

[b)]Corresponding author: rsgold@umich.edu

August 15, 2024

Abstract

We have investigated the origins of photoluminescence from quantum dots (QD) layers prepared by alternating depositions of sub-monolayers and a few monolayers of size-mismatched species, termed sub-monolayer (SML) epitaxy, in comparison with their Stranski-Krastanov (SK) QD counterparts. Using measured nanostructure sizes and local In-compositions from local-electrode atom probe (LEAP) tomography as input into self-consistent Schrödinger-Poisson simulations, we compute the 3D confinement energies, probability densities, and photoluminescence (PL) spectra for both InAs/GaAs SML- and SK-QD layers. A comparison of the computed and measured PL spectra suggests one-dimensional electron confinement, with significant 3D hole localization in the SML-QD layers that contribute to their enhanced PL efficiency in comparison to their SK-QD counterparts.

Self-assembled Stranski-Krastanov quantum dots (SK-QDs)[1,2] are often proposed for novel optoelectronic devices due to their ability to confine carriers in three dimensions (3D), in contrast to the one-dimensional (1D) confinement of quantum wells (QWs). Due to their absorption of normal-incidence radiation, as well as their reduced dark currents and higher detectivities, SK-QDs are often used in place of QWs in infrared photodetectors.[3–7] Furthermore, in principle, the 3D confinement in SK-QDs enables the splitting of quasi-Fermi levels,[8,9] as needed for intermediate band solar cells (IBSCs). However, the observed lower open-circuit voltage and efficiencies for SK-QD IBSCs in comparison to their QW counterparts,[10,11] have limited their use in solar cells.

It has been suggested that InAs/GaAs sub-monolayer quantum dots (SML-QDs), consisting of alternating depositions of sub-monolayers and a few monolayers of size-mismatched species, result in stacks of vertically-aligned 1-ML-height islands with 3D carrier confinement. Remarkably, InAs/GaAs SML-QDs have led to a higher open-circuit voltage and higher efficiency in solar cells,[10–15] higher detectivity in infrared photodetectors,[6,7,16,17] and lower threshold current and higher output power in lasers compared to SK-QDs and QWs.[18–21] It is often suggested that the enhanced performance of SML-QD devices is due to 3D confinement of both electrons and holes in columnar nanostructures.[6,7,15] Meanwhile, two-dimensional (2D) cross-sectional scanning tunneling microscopy (XSTM) suggests that SML-QDs consist of $In_xGa_{1-x}As$ clusters embedded in an $In_yGa_{1-y}As$/GaAs QW with lower In composition ($x>y$),[22,23] although the precise x and y values remain unknown. Using 2D projections of nanostructure sizes and local indium compositions from XSTM as input into Schrödinger-Poisson simulations, it has been instead suggested that electrons are confined in 1D, with holes localized in 3D.[13,23] Since realistic calculations involving the 3D topology and In compositions have yet to be performed, the influence of the 3D nanostructure of InAs/GaAs SML-QDs on their electronic states and optical properties remain unknown.

Here, we report on the origins of PL from InAs/GaAs SML-QD layers. We use the 3D topology and local In compositions, x_{In}, from local electrode atom probe tomography (LEAP) as input into self-consistent Schrödinger-Poisson simulations of 3D confinement energies, probability densities, and photoluminescence (PL) spectra for both SML-QDs and SK-QDs. This work provides important insight into the origins of the enhanced PL efficiency for SML-QDs in comparison to their SK-QDs counterparts, providing a pathway for high efficiency optoelectronics and photovoltaics.

For these studies, SML-QDs and "reference" SK-QDs were prepared using molecular-beam epitaxy, using the substrate temperatures and growth rates described in the Supplementary Material. For LEAP studies, heterostructures consisting of multiple sets of QD layers, each separated by ~40 nm thick GaAs spacer layers, intended to prevent coupling between QD layers, were prepared by molecular-beam epitaxy (MBE). Multiple conical-shaped LEAP specimens ("tips") were prepared from 3 different epitaxial samples that contained a total of 22 distinct QD layers, a subset of which are discussed in this paper. These QD layers are buried at least 500nm from the top surface of each epitaxial heterostructure. Since the thickness of the QD capping layers influences the emission intensities, separate PL samples, each containing SK or SML-QDs, with otherwise identical layer structures, including 50 nm capping layers, were prepared. Here, we discuss three types of QD layers: InAs/GaAs SML-QD layers consisting of 6 repeats of 0.5ML InAs followed by 2.5 ML GaAs formed on either c(4×4) or (2×4) GaAs(001) surfaces, as well as InAs/GaAs SK-QD layers obtained from deposition of 2.2 MLs of InAs on a c(4×4) GaAs(001) surface. For simplicity, we refer to these nanostructures as c(4×4) SML-QD, (2×4) SML-QD, and

SK-QD layers, respectively. For the SML-QD layers, we consider both (2×4) and c(4×4) surface reconstructions, allowing comparison with both our SK-QD and those SML-QD layers from earlier reports suggesting that 2D island formation growth with the (2×4) reconstruction.[24,25]

For LEAP studies, samples were coated with a 500-nm thick Pt layer, welded onto a silicon post, milled into conical shapes ("tips") using a focused-ion beam,[26] and loaded into the Cameca LEAP 5000XR, which is maintained at cryogenic temperatures (<25 K) under ultra-high vacuum conditions (3.0×10^{-11} Torr). LEAP experiments were performed in laser mode with a wavelength of 355 nm, pulse energy of 1 pJ, pulse frequency of 100 kHz, and detection rate of 0.005 atom/pulse. For the three types of QDs, the total region-of-interest (ROI) volumes exceeded 80,000 nm^3. 3D reconstructions of LEAP datasets were produced using Cameca's Integrated Visualization and Analysis software (IVAS) in AP Suite 6.3 The PL spectra were acquired at 50 K using a 19.2 μW solid-state laser emitting at 730 nm and a Si CCD (InGaAs diode-array detector) for SML-QDs (SK-QDs). Finally, using the nanostructure volumes and local x_{In} values from LEAP, probability densities, confined state energies, and photoluminescence spectra were computed using 3D Schrödinger-Poisson simulations in the effective mass approximation at 50 K using nextnano.

To examine In incorporation and visualize InGaAs clusters and QDs within the QD layers, we present x-z views of LEAP reconstructions containing the (2×4) SML-QD layers (Fig. 1(a)), the c(4×4) SML-QD layer (Fig. 2(a)), and the SK-QD layers (Fig. 3(a)). The corresponding spatially-averaged 1D profiles of x_{In}, reveal maximum x_{In} values of 0.12, 0.19, and 0.18 for (2×4) SML-QD, c(4×4) SML-QD, and SK-QD layers, with $x_{In} < 0.0005$ within the GaAs spacer regions. Meanwhile, 2D contour plots, with local x_{In} values averaged over 2-nm regions of interest (ROI) vertically-centered about each QD layer, reveal ~5 nm-sized $In_xGa_{1-x}As$ clusters embedded in $In_yGa_{1-y}As$ QWs ($y < x$), for the SML-QD layers (Figs. 1(b) and 2(b)) and ~20nm-sized In_xGa_{1-}

$_x$As QDs atop wetting layers (WL) for the SK-QD layers (Fig. 3(b)), consistent with earlier XSTM reports.[22,23,27] The apparent drop in x_{In} at the edges in (b) is due to a LEAP analysis artifact related to the limited counts available for the 2D contour plots.

The process for developing nanostructural models for input into the Schrödinger-Poisson-continuity simulations is illustrated by x-y isosurfaces for each type of QD layer in Figs. 1-3. For the (2×4) SML-QDs, x-y isosurfaces with $x_{In} > 0.09$ (Fig. 1(c)) and $x_{In} > 0.14$ (Fig. 1(d)) reveal the presence of 4-5 nm $In_xGa_{1-x}As$ ($x > 0.14$) clusters embedded in an $In_yGa_{1-y}As$ quantum well ($y \approx 0.09$). For the c(4×4) SML-QD layers, x-y isosurfaces with $x_{In} > 0.14$ (Fig. 2(c)) and $x_{In} > 0.21$ (Fig. 2(d)) reveal 5-6 nm $In_xGa_{1-x}As$ ($x > 0.21$) clusters embedded in an $In_yGa_{1-y}As$ quantum well ($y \approx 0.14$). For the SK-QD layers, x-y isosurfaces with $x_{In} > 0.18$ (Fig. 3(c)) and $x_{In} > 0.42$ (Fig. 3(d)) reveal ~20nm $In_xGa_{1-x}As$ QDs ($x > 0.18$) with higher composition (up to $x \approx 0.6$) "cores". For each isosurface, all clusters with sizes ≥ 4.2 nm^3 and their local $x_{In}(x, y, z)$ were identified. To quantify local x_{In} values within In-rich clusters (or QDs) and the surrounding QWs (or WLs), we analyzed 2D contour plots from seven 1-nm thick ROI spanning each type of QD layer. For the 2D regions (QWs or WLs), the clusters were excluded from the analysis; a series of 2D contour plots shifted in the z-direction were used to obtain $\langle x_{In}(z)\rangle_{xy}$. For each cluster, we use $x_{In}(x, y, z)$ to model a series of ellipsoids as described in the supplementary materials.

For each type of QD layer, the conduction-band edge (CBE), valence-band edge (VBE), and confined states computed along the black dotted lines intersecting clusters in Figs. 1(c), 2(c), and 3(c) are shown in Figs. 4 (a)-(c), with the main findings summarized in Table S4. For each of the x, y, and z directions, if the electron (hole) level is below (above) the edge of the QW conduction (valence) band, the carrier is considered to be confined. For the SK-QD layers, the computed CBE and VBE band diagrams along the x-direction reveal that E_{e1} (E_{hh1}) lies 100 (115) meV below (above) the CBE (VBE) of the surrounding WL (x_{In} = 0.05) and 35 (65) meV below (above) the CBE (VBE) of the WL with x_{In} = 0.14. Along z-direction, E_{e1} (E_{hh1}) lies 30 (70) meV below (above) the CBE (VBE) of the surrounding WL. Thus, 3D confinement of both electrons and holes in SK-QD is confirmed. On the other hand, for the (2×4) SML-QD layers, E_{e1} (E_{hh1}) is 28 (21) meV above (below) the CBE (VBE) of the surrounding QW along the x-direction, with E_{e1} (E_{hh1}) is 20 (41) meV above (below) the CBE (VBE) of the surrounding QW along the z-direction. Similarly, for the c(4×4) SML-QD layers, E_{e1} (E_{hh1}) is 42 (27) meV above (below) the CBE (VBE), with E_{e1} (E_{hh1}) is 28 (35) meV above (below) the CBE (VBE) along the z-direction. Therefore, for the SML-QD layers, 1D carrier confinement is apparent, similar to the QW case, in contrast to assumptions of 3D confinement inferred from XSTM and PL data.[15,23,28]

To confirm the hypothesis of 1D carrier confinement in SML-QD layers, we computed electron and heavy-hole probability densities for each type of QD layer (Fig. 5), quantifying carrier "localization" as the fraction of probability density that is inside the clusters or QDs. A padding of 15 nm is added to all sides of simulation area (full size = 55 × 55 nm^2) to minimize the truncation of probability densities induced by Dirichlet boundary condition. For the SK-QD layers in Fig. 5(c), both electrons and heavy-holes are localized to the In-rich clusters, consistent with earlier reports.[29,30] On the other hand, for both types of SML-QD layers, the electron probability densities are distributed across and modulated by several In-rich clusters (see 1D probability densities profile insets), while the heavy-hole probability densities are localized to certain In-rich clusters, suggesting a "quasi-1D" carrier confinement. The localization of heavy-holes is more significant than that of electrons, presumably due to their substantially higher effective masses. For the In-rich clusters indicated by arrows in Fig. 5, the fractions of heavy-hole probability density within 10 nm^3 are 0.20 and 0.38 for the (2×4) and c(4×4) SML-QD layers. The increase in heavy-hole localization for the c(4×4) SML-QD layers is likely due to the larger cluster sizes and higher x_{In} values.

We next compute the spontaneous emission vs. energy for comparison with the measured values of PL intensity vs energy for the QD layers. For these calculations, both the ground states, shown in Figs. 4(a) - 4(c), plus the excited states, shown in the Supplementary Material, were included. Figure 5 presents the measured (solid) and computed (dashed) PL data for the SK-QD layers (green), c(4×4) SML-QD layers (blue), and the (2×4) SML-QD layers (red). Similar trends in the relative PL emission energies and emission intensities are observed for the measured and computed PL data, with emission intensities increasing from c(4×4) SML-QD layers (blue) to SK-QD layers (green) to (2×4) SML-QD layers (red). For each type of QD layer, the systematic blue-shift (to higher energy) of the computed PL emission energies with respect to the measured values may be due to the higher thickness of the overgrown layers (≥ 500 nm for LEAP structures vs. 50 nm for PL structures) grown at temperatures sufficiently high to generate In out-diffusion.[31-33] Thus, for the QD layers within the LEAP structures, the lower In concentrations would lead to higher computed PL emission energies. Furthermore, although both SML-QD and SK-QD layers exhibit compositional inhomogeneities, the quasi-1D confinement in the SML-QD layers leads to narrower emission linewidths typical of QWs.[34] To understand the trends in PL emission intensities, we consider both the real-space overlap of the electron-heavy-hole probability densities[35-37] (i.e. the transition intensity) and the total number of states contributing to the emission.

For the SK-QD layers, the probability densities are confined inside the QDs, resulting in significant real-space overlap of the electron-heavy-hole probability densities, but only ground state electrons and heavy-holes contribute to the emission. On the other hand, for both types of

SML-QD layers, the electron probability densities are distributed across several In-rich clusters while the heavy-hole probability densities are localized in the vicinity of certain In-rich clusters. However, as mentioned above, for the (2×4) SML-QD layers, there are 3 electron and 7 heavy-hole states contributing to the emission (see Table S5 of Supplementary Material) which ultimately leads to the high PL emission intensity of the (2×4) SML-QD layers. The emission intensity of the c(4×4) SML-QD layers is predominantly determined by their improved heavy hole localization that decreases the real-space overlap of the electron-hole probability densities, causing the emission of c(4×4) SML-QD layers to be less intense than that of the SK-QD layers despite the number of states contributing to total emission.

In summary, we examined the origins of the narrow and intense PL emission from InAs/GaAs SML-QD layers—similar to that of a QW—in contrast to the broader and weaker PL emission typical of SK-QD layers. Using realistic 3D nanostructure sizes and local InGaAs composition profiles from LEAP as input into self-consistent Schrödinger-Poisson simulations of SML-QD and SK-QD layers, we demonstrated 1D electron confinement with significant 3D hole localization in the SML-QD layers, in contrast to 3D confinement of electrons and holes in SK-QD layers. In other words, SML-QD layers are not strictly three-dimensionally-confined "quantum dots".[38] Despite the significant real-space overlap of the electron-heavy-hole probability densities in SK-QD layers, SML-QD layers have a larger number of states contributing to their emission, resulting in higher PL intensities. Furthermore, the real-space overlap of the electron-heavy-hole probability densities and the total number of states is greatest for the (2×4) SML-QD layers, leading to their higher PL emission intensity. This work provides important insight into the origins of the enhanced PL efficiency for SML-QD layers in comparison to their SK-QD counterparts.

Supplementary materials

The parameters used for molecular-beam epitaxy of InAs/GaAs SML-QD and SK-QD layers, including the shutter sequences, the elemental incorporation rates (IR), and the substrate temperatures for all layers, are described in the supplemental materials. In addition, the isosurface threshold selection criteria and nextnano model development are described. Next, we present LEAP data, as well as the computed probability density and energy band diagram for the reference QW. Finally, the computed excited-state probability densities for the SML-QD and SK-QD layers, and a comparison of the real-space overlap of the electron-heavy-hole probability densities (i.e. the transition intensities) for all combinations of confined and excited states are presented.

Acknowledgement

We gratefully acknowledge support from the National Science Foundation (Grant No. DMR 1810280). T.-Y. Huang, T. Borrely, and R.S. Goldman were supported in part by the Air Force Office of Scientific Research through the Multidisciplinary University Research Initiative, Award No. FA9550-23-1-0334. This study was financed in part by the Coordenação de Aperfeiçoamento de Pessoal de Nível Superior – Brasil (CAPES) – Finance Code 001. T.-Y. Huang and Y.-C. Yang were also supported in part by the Chia-Lun Lo Fellowship from the Rackham Graduate School at the University of Michigan. The authors acknowledge the financial support of the Fundação de Amparo à Pesquisa do Estado de São Paulo (FAPESP) - grant # 2022/10340-2.

Captions

Fig. 1: LEAP data for (2x4) SML-QD layers: (a) x-z view of LEAP reconstruction, with corresponding spatially-averaged 1D profiles of x_{In}, (b) 2D contour plots, and x-y isosurfaces for (c) $x_{In} > 0.09$ and (d) $x_{In} > 0.14$. The horizontal black dotted line in the top of (d) indicates the position of the x-z isosurface shown in the bottom of (d). The region outlined by the black square in (d) was used for the nextnano simulations.

Fig. 2: LEAP data for the c(4x4) SML-QD layers: (a) x-z view of LEAP reconstruction, with corresponding spatially-averaged 1D profiles of x_{In}, (b) 2D contour plots, and x-y isosurfaces for (c) $x_{In} > 0.14$ and (d) $x_{In} > 0.28$. The horizontal black dotted line in the top of (d) indicates the position of the x-z isosurface shown in the bottom of (d). The region outlined by the black square in (d) was used for the nextnano simulations.

Fig. 3: LEAP data for the SK-QD layer: (a) x-z view of LEAP reconstruction, with corresponding spatially-averaged 1D profiles of x_{In}, (b) 2D contour plots, and x-y isosurfaces for (c) $x_{In} > 0.18$ and (d) $x_{In} > 0.42$. The horizontal black dotted line in the top of (d) indicates the position of the x-z isosurface shown in the bottom of (d). The region outlined by the black square in (d) was used for the nextnano simulations.

Fig. 4: The x- and z-dependence of the conduction-band edge (CBE) (black), valence-band edge (VBE) (black), and confined states (colorful) for the (a) (2×4) SML-QD, (b) c(4×4) SML-QD and (c) SK-QD layers, computed along the black dotted lines intersecting clusters in Figs. 1(d), 2(d), and 3(c). The z-dependence of the CBE and VBE of the clusters/QDs are marked in orange.

Fig. 5: Computed probability densities of the ground state electrons (e1) and heavy-holes (hh1) for (a) (2×4) SML-QDs, (b) c(4×4) SML-QDs, and (c) SK-QDs. The white dotted circles/ovals indicate the positions of clusters/dots, and the maximum value of the color scale is shown in the

upper right corner. The arrows indicate the In-rich clusters used to quantify the localization of heavy-hole probability densities of the SML-QDs. The insets to the ground state electrons (e1) illustrate the 1D probability densities along the black dotted lines in (a), (b), and (c).

Fig. 6: Measured (solid lines) and computed (dashed lines) PL emission vs energy for the SK-QDs (green), c(4×4) SML-QDs (blue), and (2×4) SML-QDs (red). The energy of the maximum of each spectrum is indicated. For the SK-QDs, the linewidth of the simulated PL is narrow due to the inclusion of only one QD in the simulation.

Figure 1

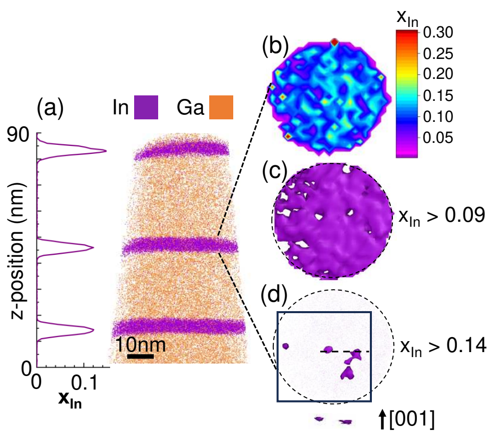
(a)
In
Ga
90
0
z-position (nm)
0
0.1
x_In
10nm
(b)
x_In
0.30
0.25
0.20
0.15
0.10
0.05
(c)
x_In > 0.09
(d)
x_In > 0.14
[001]

Figure 2

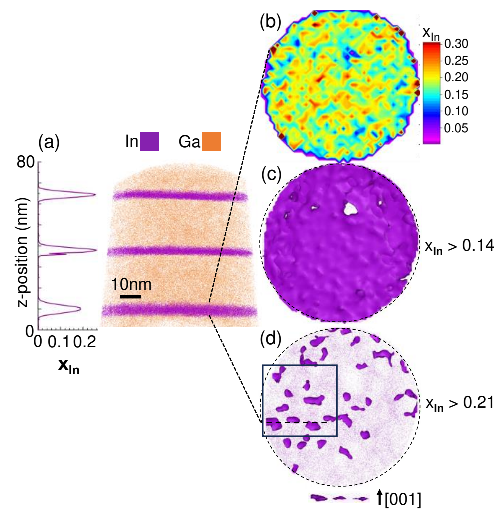
(a)
In
Ga
80
0
z-position (nm)
0 0.1 0.2
x_{In}
10nm
(b)
x_{In}
0.30
0.25
0.20
0.15
0.10
0.05
(c)
x_{In} > 0.14
(d)
x_{In} > 0.21
[001]

Figure 3

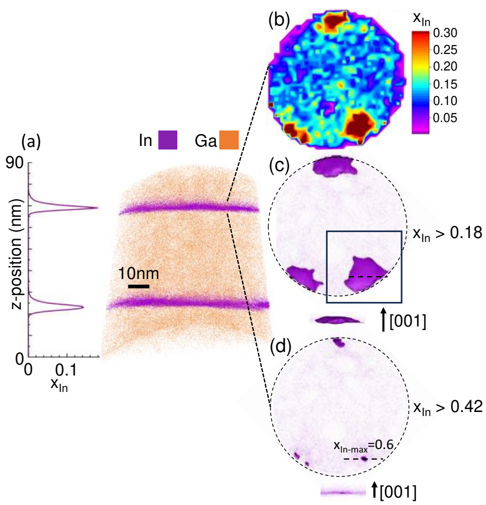
(a)
In
Ga
90
z-position (nm)
10nm
0
0
0.1
x_{In}
(b)
x_{In}
0.30
0.25
0.20
0.15
0.10
0.05
(c)
x_{In} > 0.18
[001]
(d)
x_{In} > 0.42
$x_{In\text{-}max}$=0.6
[001]

244

Figure 4

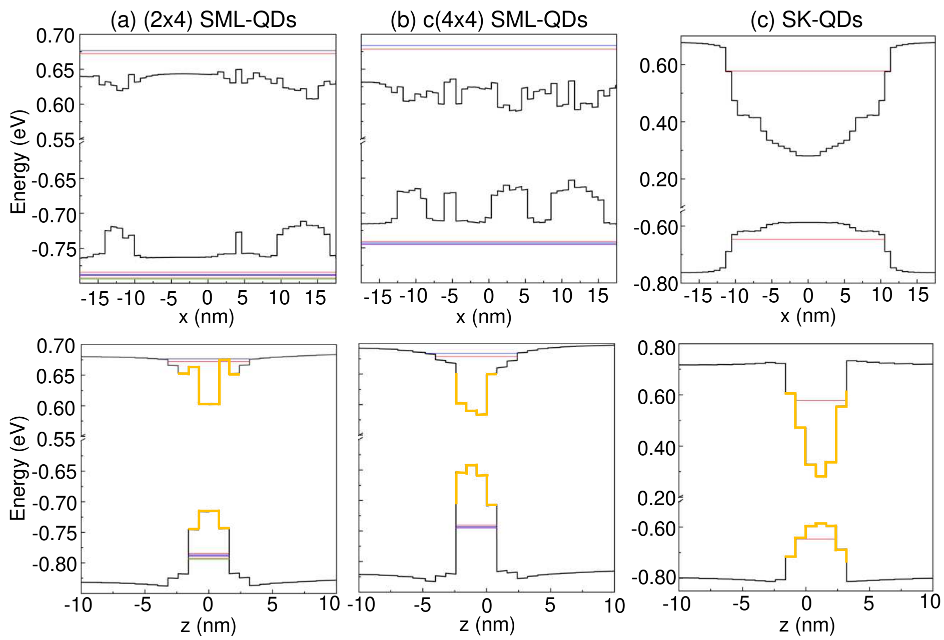

245

246 **Figure 5**

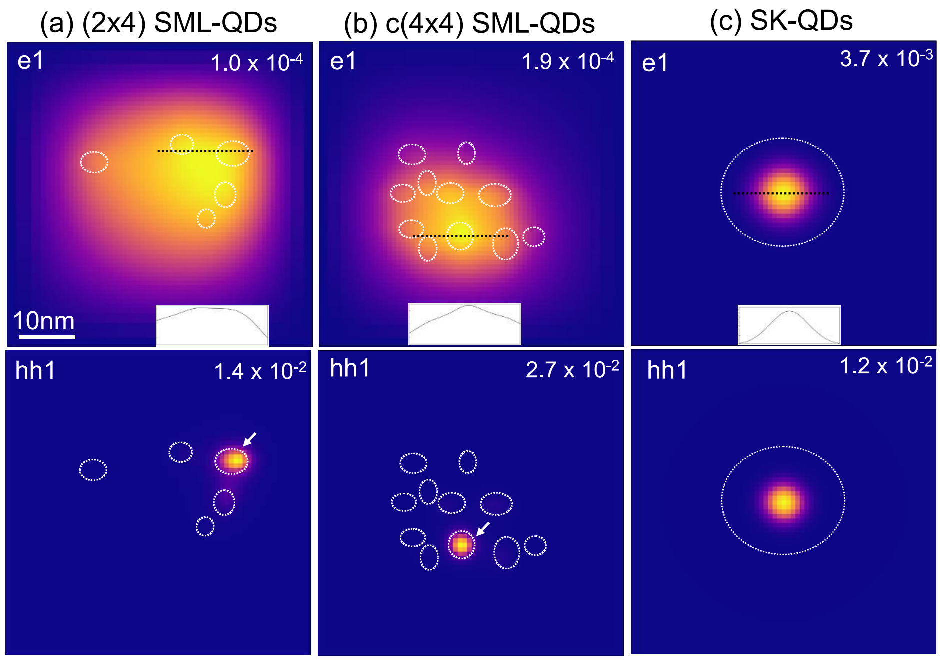

247

Figure 6

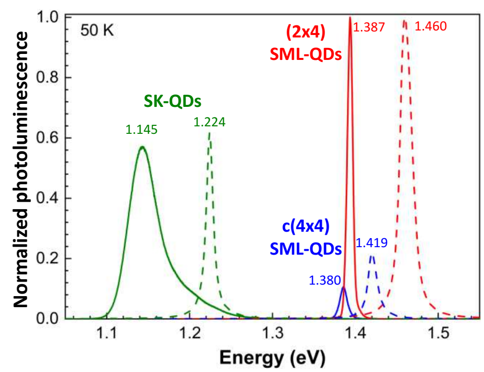
50 K
(2x4)
SML-QDs
1.387
1.460
SK-QDs
1.145
1.224
c(4x4)
SML-QDs
1.419
1.380
Normalized photoluminescence
Energy (eV)
1.0
0.8
0.6
0.4
0.2
0.0
1.1
1.2
1.3
1.4
1.5

References
[1] Í. Ramiro, J. Villa, P. Lam, S. Hatch, J. Wu, E. López, E. Antolín, H. Liu, A. Martí, and A. Luque, "Wide-Bandgap InAs/InGaP Quantum-Dot Intermediate Band Solar Cells," IEEE J. Photovolt. **5**, 840 (2015).
[2] M.J. da Silva, A.A. Quivy, S. Martini, T.E. Lamas, E.C.F. da Silva, and J.R. Leite, "Optical response at 1.3μm and 1.5μm with InAs quantum dots embedded in a pure GaAs matrix," J. Cryst. Growth **251**, 181 (2003).
[3] B.F. Levine, "Quantum-well infrared photodetectors," J. Appl. Phys. **74**, R1 (1993).
[4] X.-J. Wang, S.-Q. Zhai, N. Zhuo, J.-Q. Liu, F.-Q. Liu, S.-M. Liu, and Z.-G. Wang, "Quantum dot quantum cascade infrared photodetector," Appl. Phys. Lett. **104**, 171108 (2014).
[5] M.P. Touse, G. Karunasiri, K.R. Lantz, H. Li, and T. Mei, "Near- and mid-infrared detection using GaAs∕InxGa1−xAs∕InyGa1−yAs multiple step quantum wells," Appl. Phys. Lett. **86**, 093501 (2005).
[6] J.O. Kim, S. Sengupta, A.V. Barve, Y.D. Sharma, S. Adhikary, S.J. Lee, S.K. Noh, M.S. Allen, J.W. Allen, S. Chakrabarti, and S. Krishna, "Multi-stack InAs/InGaAs sub-monolayer quantum dots infrared photodetectors," Appl. Phys. Lett. **102**, 011131 (2013).
[7] S. Sengupta, J.O. Kim, A.V. Barve, S. Adhikary, Y.D. Sharma, N. Gautam, S.J. Lee, S.K. Noh, S. Chakrabarti, and S. Krishna, "Sub-monolayer quantum dots in confinement enhanced dots-in-a-well heterostructure," Appl. Phys. Lett. **100**, 191111 (2012).
[8] S.R. Tatavarti, Z.S. Bittner, A. Wibowo, M.A. Slocum, G. Nelson, H. Kum, S.P. Ahrenkiel, and S.M. Hubbard, "Epitaxial Lift-off (ELO) of InGaP/GaAs/InGaAs solar cells with quantum dots in GaAs middle sub-cell," Sol. Energy Mater. Sol. Cells **185**, 153 (2018).
[9] G. Yang, W. Liu, Y. Bao, X. Chen, C. Ji, B. Wei, F. Yang, and X. Wang, "Performance optimization of In(Ga)As quantum dot intermediate band solar cells," Discover Nano **18**, 67 (2023).
[10] N. Alnami, R. Kumar, A. Kuchuk, Y. Maidaniuk, S.K. Saha, A.A. Alnami, R. Alhelais, A. Kawagy, M.E. Ware, Y.I. Mazur, and G.J. Salamo, "InAs nanostructures for solar cell: Improved efficiency by submonolayer quantum dot," Sol. Energy Mater. Sol. Cells **224**, 111026 (2021).
[11] N. Alnami, R. Kumar, S. Saha, A. Alnami, M.E. Ware, Y.I. Mazur, and G.J. Salamo, "Temperature dependent behavior of sub-monolayer quantum dot based solar cell," Sol. Energy Mater. Sol. Cells **259**, 112448 (2023).
[12] I.S. Han, J.S. Kim, J.O. Kim, S.K. Noh, and S.J. Lee, "Fabrication and characterization of InAs/InGaAs sub-monolayer quantum dot solar cell with dot-in-a-well structure," Curr. Appl. Phys. **16**, 587 (2016).
[13] T. Borrely, A. Alzeidan, M.D. de Lima, G.M. Jacobsen, T.-Y. Huang, Y.-C. Yang, T.F. Cantalice, R.S. Goldman, M.D. Teodoro, and A.A. Quivy, "Viability of intermediate band solar cells based on InAs/GaAs submonolayer quantum dots and the role of surface reconstruction," Sol. Energy Mater. Sol. Cells **254**, 112281 (2023).
[14] A. Chatterjee, D. Das, J. Patwari, B. Tongbram, D. Panda, S. Chakrabarti, and S.K. Pal, "Ultrafast electronic spectroscopy on the coupling of Stranski-Krastanov and submonolayer quantum dots for potential application in near infrared light harvesting," Mater. Res. Express **6**, 085903 (2019).
[15] P. Lam, J. Wu, M. Tang, Q. Jiang, S. Hatch, R. Beanland, J. Wilson, R. Allison, and H. Liu, "Submonolayer InGaAs/GaAs quantum dot solar cells," Sol. Energy Mater. Sol. Cells **126**, 83 (2014).

[16] A. Alzeidan, T.F. Cantalice, K.D. Vallejo, R.S.R. Gajjela, A.L. Hendriks, P.J. Simmonds, P.M. Koenraad, and A.A. Quivy, "Effect of As flux on InAs submonolayer quantum dot formation for infrared photodetectors," Sens. Actuator A Phys. **334**, 113357 (2022).
[17] S. Mukherjee, S. Mukherjee, A. Pradhan, T. Maitra, S. Sengupta, S. Chakrabarti, A. Nayak, and S. Bhunia, "Carrier transport and recombination dynamics of InAs/GaAs sub-monolayer quantum dot near infrared photodetector," J. Phys. D: Appl. Phys. **52**(50), 505107 (2019).
[18] H.-P.D. Yang, I.-C. Hsu, Y.-H. Chang, F.-I. Lai, H.-C. Yu, G. Lin, R.-S. Hsiao, N.A. Maleev, S.A. Blokhin, H.-C. Kuo, and J.Y. Chi, "Characteristics of InGaAs Submonolayer Quantum-Dot and InAs Quantum-Dot Photonic-Crystal Vertical-Cavity Surface-Emitting Lasers," J. Lightwave Technol. **26**, 1387 (2008).
[19] T.D. Germann, A. Strittmatter, U.W. Pohl, D. Bimberg, J. Rautiainen, M. Guina, and O.G. Okhotnikov, "Quantum-dot semiconductor disk lasers," J. Cryst. Growth. **310**, 5182 (2008).
[20] S.S. Mikhrin, A.E. Zhukov, A.R. Kovsh, N.A. Maleev, V.M. Ustinov, Y.M. Shernyakov, I.P. Soshnikov, D.A. Livshits, I.S. Tarasov, D.A. Bedarev, B.V. Volovik, M.V. Maximov, A.F. Tsatsul'nikov, N.N. Ledentsov, P.S. Kop'ev, D. Bimberg, and Z.I. Alferov, "0.94 µm diode lasers based on Stranski-Krastanow and sub-monolayer quantum dots," Semicond. Sci. Technol. **15**, 1061 (2000).
[21] V.M.U. Alferov A.R. Kovsh, D.A. Livshits, A.E. Zhukov, A. Yu Egorov, M.V. Maximov, I.S. Tarasov, N.N. Ledentsov, P.S. Kop`ev, Zh I., "High output power CW operation of a quantum dot laser.," in *Compound Semiconductors 1999*, (CRC Press, 2000).
[22] R.S.R. Gajjela, A.L. Hendriks, A. Alzeidan, T.F. Cantalice, A.A. Quivy, and P.M. Koenraad, "Cross-sectional scanning tunneling microscopy of InAs/GaAs(001) submonolayer quantum dots," Phys. Rev. Mater. **4**, 114601 (2020).
[23] S. Harrison, M.P. Young, P.D. Hodgson, R.J. Young, M. Hayne, L. Danos, A. Schliwa, A. Strittmatter, A. Lenz, H. Eisele, U.W. Pohl, and D. Bimberg, "Heterodimensional charge-carrier confinement in stacked submonolayer InAs in GaAs," Phys. Rev. B **93**, 085302 (2016).
[24] J.G. Belk, C.F. McConville, J.L. Sudijono, T.S. Jones, and B.A. Joyce, "Surface alloying at InAs/GaAs interfaces grown on (001) surfaces by molecular beam epitaxy," Surf. Sci. **387**, 213 (1997).
[25] G.R. Bell, T.J. Krzyzewski, P.B. Joyce, and T.S. Jones, "Island size scaling for submonolayer growth of InAs on GaAs(001)-(2×4): Strain and surface reconstruction effects," Phys. Rev. B **61**, R10551 (2000).
[26] T. Borrely, T.-Y. Huang, Y.-C. Yang, R.S. Goldman, and A.A. Quivy, "On the importance of atom probe tomography for the development of new nanoscale devices," in *2022 36th Symposium on Microelectronics Technology (SBMICRO)*, (2022), pp. 1–4.
[27] J.G. Keizer, A.B. Henriques, A.D.B. Maia, A.A. Quivy, and P.M. Koenraad, "Atomically resolved study of the morphology change of InAs/GaAs quantum dot layers induced by rapid thermal annealing," Appl. Phys. Lett. **101**, 243113 (2012).
[28] T.F. Cantalice, A. Alzeidan, G.M. Jacobsen, T. Borrely, M.D. Teodoro, and A.A. Quivy, "Evidence of weak strain field in InAs/GaAs submonolayer quantum dots," Micro Nanostructures **172**, 207449 (2022).
[29] R.C. Roca, and I. Kamiya, "Photoluminescence tuning of stacked submonolayer (SML) InAs nanostructures across the 2D to 3D transition," Appl. Phys. Lett. **118**, 183104 (2021).
[30] R.C. Roca, and I. Kamiya, "Structural investigation of the 2D to 3D transition in stacked submonolayer InAs nanostructures," AIP Advances **11**, 075011 (2021).

[31] B. Lita, R.S. Goldman, J.D. Phillips, and P.K. Bhattacharya, "Interdiffusion, segregation, and dissolution in InAs/GaAs quantum dot superlattices," Surf. Rev. Lett. **07**, 539 (2000).
[32] B. Lita, R.S. Goldman, J.D. Phillips, and P.K. Bhattacharya, "Nanometer-scale studies of vertical organization and evolution of stacked self-assembled InAs/GaAs quantum dots," Appl. Phys. Lett. **74**, 2824 (1999).
[33] B. Lita, R.S. Goldman, J.D. Phillips, and P.K. Bhattacharya, "Interdiffusion and surface segregation in stacked self-assembled InAs/GaAs quantum dots," Appl. Phys. Lett. **75**, 2797 (1999).
[34] R.C. Roca, and I. Kamiya, "Change in Topography of InAs Submonolayer Nanostructures at the 2D to 3D Transition," Phys Status Solidi (b) **258**, 2170012 (2021).
[35] C.A. Duarte, E.C.F. da Silva, A.A. Quivy, M.J. da Silva, S. Martini, J.R. Leite, E.A. Meneses, and E. Lauretto, "Influence of the temperature on the carrier capture into self-assembled InAs/GaAs quantum dots," J. Appl. Phys. **93**, 6279 (2003).
[36] A.M. Ceschin, A.A. Quivy, J.A.N.T. Soares, R. Enderlein, A. Tabata, L.M.R. Scolfaro, E.C.F. da Silva, J.R. Leite, J.B.B. Oliveira, and E.A. Meneses, "Photoluminescence and photoreflectance studies on δ-Doped $In_{0.15}Ga_{0.85}As$/GaAs quantum wells," Superlattices Microstruct. **15**, 333 (1994).
[37] A. Tabata, A.M. Ceschin, A.A. Quivy, A. Levine, J.R. Leite, R. Enderlein, J.B.B. Oliveira, E. Laureto, and J.L. Gonçalves, "Investigation of the photoluminescence linewidth broadening in symmetric and asymmetric InGaAsGaAs n-type δ-doped quantum wells," MSEB **35**, 401 (1995).
[38] D. Bimberg, and U.W. Pohl, "Quantum dots: promises and accomplishments," Mater. Today **14**, 388 (2011).